

Broadband terahertz transmissive quarter-wave metasurface

Cite as: APL Photonics 5, 096108 (2020); <https://doi.org/10.1063/5.0017830>

Submitted: 10 June 2020 . Accepted: 28 August 2020 . Published Online: 17 September 2020

 Xiaolong You,  Rajour T. Ako,  Wendy S. L. Lee,  Madhu Bhaskaran,  Sharath Sriram,  Christophe Fumeaux, and  Withawat Withayachumnankul

COLLECTIONS

Paper published as part of the special topic on [2020 Future Luminary Collection](#)



ARTICLES YOU MAY BE INTERESTED IN

[Ultra-wideband tri-layer transmissive linear polarization converter for terahertz waves](#)
APL Photonics 5, 046101 (2020); <https://doi.org/10.1063/1.5144115>

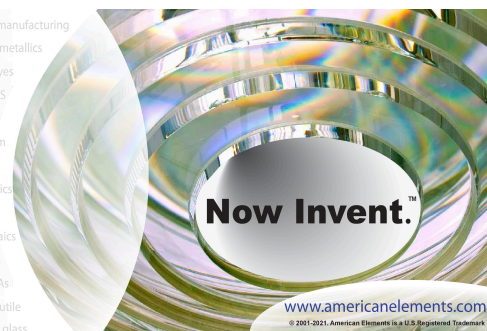
[Deep learning of ultrafast pulses with a multimode fiber](#)
APL Photonics 5, 096106 (2020); <https://doi.org/10.1063/5.0007037>

[Broadband and wide-angle reflective linear polarization converter for terahertz waves](#)
APL Photonics 4, 096104 (2019); <https://doi.org/10.1063/1.5116149>



yttrium iron garnet glassy carbon beamsplitters fused quartz additive manufacturing
zeolites III-IV semiconductors gallium lump copper nanoparticles organometallics
nano ribbons barium fluoride europium phosphors photonics infrared dyes
epitaxial crystal growth ultra high purity materials transparent ceramics CIGS
cerium oxide polishing powder surface functionalized nanoparticles MRE grade materials thin film
sapphire windows Nd:YAG silver nanoparticles perovskites MOCVD beta-barium borate
rare earth metals quantum dots osmium scintillation Ce:YAG refractory metals laser crystals
anode lithium niobate InAs wafers dysprosium pellets MOFs AuNPs chalcogenides ZnS CdTe
perovskite crystals transparent ceramics

The Next Generation of Material Science Catalogs



Broadband terahertz transmissive quarter-wave metasurface

Cite as: APL Photon. 5, 096108 (2020); doi: 10.1063/5.0017830

Submitted: 10 June 2020 • Accepted: 28 August 2020 •

Published Online: 17 September 2020









View Online



Export Citation



CrossMark

Xiaolong You,¹  Rajour T. Ako,²  Wendy S. L. Lee,¹  Madhu Bhaskaran,²  Sharath Sriram,² 
Christophe Fumeaux,¹  and Withawat Withayachumnankul^{1,a)} 

AFFILIATIONS

¹Terahertz Engineering Laboratory, School of Electrical and Electronic Engineering, The University of Adelaide, Adelaide SA 5005, Australia

²Functional Materials and Microsystems Research Group and The Micro Nano Research Facility, RMIT University, Melbourne VIC 3001, Australia

^{a)} Author to whom correspondence should be addressed: withawat@adelaide.edu.au

ABSTRACT

Polarization conversion devices are key components in spectroscopy and wireless communications systems. Conventional terahertz waveplates made of natural birefringent materials typically suffer from low efficiency, narrow bandwidth, and substantial thickness. To overcome the limitations associated with conventional waveplates, a terahertz quarter-wave metasurface with enhanced efficiency and wide bandwidth is proposed. The transmissive quarter-wave metasurface is rigorously designed based on an extended semi-analytical approach employing network analysis and genetic algorithm. Simulation results suggest that the design can achieve linear-to-circular polarization conversion with a 3-dB axial ratio relative bandwidth of 53.3%, spanning 205 GHz–354 GHz. The measurement results confirm that the proposed design enables a 3-dB axial ratio from 205 GHz to at least 340 GHz with a total efficiency beyond 70.2%, where the upper frequency bound is limited by the available experimental facility. This quarter-wave metasurface can cover an entire terahertz electronics band and can be scaled to cover other nearby bands under the same convention, which are technologically significant for future portable systems.

© 2020 Author(s). All article content, except where otherwise noted, is licensed under a Creative Commons Attribution (CC BY) license (<http://creativecommons.org/licenses/by/4.0/>). <https://doi.org/10.1063/5.0017830>

I. INTRODUCTION

The terahertz spectral range defined between 0.1 THz and 10 THz¹ presents a unique potential for diverse applications, including wireless communications,^{2,3} medical imaging,^{4,5} and substance identification.⁶ In order to harness the terahertz waves for those applications, various terahertz devices have been developed, such as modulators,⁷ filters,⁸ and antennas.^{3,9} Waveplates that alter the polarization state of incident beams provide additional degrees of freedom to manipulate the terahertz waves.

Birefringent materials such as crystalline dielectrics^{10,11} and wood¹² provide distinct refractive indices to electric field components along two orthogonal directions, thus leading to different phase accumulations. By carefully controlling the thickness of a birefringent material, a prescribed phase difference between the two electric field components can be achieved at a given frequency. However, waveplates made of quartz using one single layer

typically feature a narrow bandwidth of ~14.4% and significant reflection and absorption losses. The multi-layer quartz-based waveplate was presented to improve the relative bandwidth to 32% but exhibited a bulky configuration and an efficiency of merely 50%.¹¹ Alternative wave-plate construction methods involving the effective medium theory^{13,14} or the form-birefringence methodology^{15,16} demand further efficiency and bandwidth enhancement. As a substitute, polarization conversions can be implemented by employing metasurfaces.

Metasurfaces formed by periodically arranged subwavelength resonators can be exploited to locally manipulate the amplitude, phase, and polarization state of waves in reflection or transmission. Metasurfaces have demonstrated their extraordinary electromagnetic properties in wavefront shaping^{17–20} and polarization control.^{21–24} More specifically relevant to this article, metasurfaces are also capable of providing designable birefringence to realize quarter-wave plates for conversion between linear and circular

polarizations. In the microwave engineering community, strip gratings were employed in a quarter-wave plate design²⁵ with a limited 3-dB axial ratio relative bandwidth of 20%. A quarter-wave plate based on reactive impedance surfaces exhibited a relative bandwidth of 40%, but the six layers of metal would be prohibitively difficult to fabricate at terahertz frequencies.²⁶ In the millimeter-wave region, a tri-layer quarter-wave plate exhibited a simulated 3-dB axial ratio fractional bandwidth of 40% and an efficiency above 59.2%.²⁷ However, the quarter-wave plate design did not involve optimization algorithms, which leaves room for performance improvement. In the terahertz domain, split ring resonators²⁸ and metal slots²⁹ have been reported to realize linear-to-circular polarization conversion with an efficiency of 62% and 30%, respectively, requiring further efficiency improvement. In the optics region, waveplates typically show low transmittance resulting from the relatively high metal losses at optical frequencies.^{30,31}

In this work, we propose a broadband transmissive quarter-wave metasurface with enhanced efficiency. The proposed design targets coverage of the WR-3.4 waveguide frequency range from 220 GHz to 330 GHz, which is foreseen for terahertz point-to-point communications.³² The transmissive quarter-wave metasurface consists of three metallic layers separated by two dielectric spacers. Each metallic layer can be modeled as a parallel LC circuit along the x - or y -polarization, while the dielectric spacers are represented by transmission lines in the z -direction. Thus, a semi-analytical approach incorporating network analysis and genetic algorithm is implemented to optimize the quarter-wave metasurface. The network analysis investigates the scattering characteristics of the anisotropic metasurface, while the genetic algorithm as an optimization algorithm is employed to determine the optimal circuit parameters for the quarter-wave metasurface to achieve a low axial ratio and high transmission over a wide bandwidth. The quarter-wave metasurface is then physically realized by designing a particular pattern for each metallic layer, which reproduces the calculated optimal circuit parameters. It is worth mentioning that the extended semi-analytical approach employed in the quarter-wave metasurface design is capable of configuring transmissive metasurfaces for other functionalities.

II. DESIGN PRINCIPLE

Here, we design a transmissive quarter-wave metasurface that comprises three metallic layers separated by two dielectric

spacers. Figure 1(a) illustrates a metasurface structure with identical top and bottom layers, and the two dielectric spacers having the same thickness. The induced currents on the middle layer generated by the $-x$ -directed quasi-static magnetic field are canceled out due to the symmetric nature of the structure.²⁷ As a result, the three metallic layers collectively interact with the electric field, while the magnetic response is shaped only by the top and bottom layers. Therefore, design priority is given to the top and bottom layers to manipulate the magnetic response first, while the middle layer is subsequently tailored for the electric response without affecting the magnetic field. Consequently, the electric and magnetic responses are controlled separately, and thus, each unit cell acts as a Huygens' source that consists of crossed electric and magnetic dipoles of equal strength. Figure 1(b) depicts the electric fields generated by the electric and magnetic dipoles, where electric fields present equal strength and opposite signs in the $z < 0$ space, but the same sign in the $z > 0$ space. As a result, a destructive interference occurs in the $z < 0$ space that leads to a reduced reflection from the metasurface, while a constructive interference happens in the $z > 0$ space that results in an improved transmission.³³ Therefore, a large transmission phase tuning range can be accomplished simultaneously with a high transmittance by properly controlling electric and magnetic dipole resonances, leading to an efficiency-enhanced metasurface.^{27,34,35}

In order to facilitate the design process and optimize the device performance, the quarter-wave metasurface is designed with the aid from an extended semi-analytical approach, which is developed on the basis of the approach presented by Pfeiffer and Grbic.^{27,36} The extended approach implemented here involves network analysis combined with a genetic algorithm to determine the optimal frequency-independent circuit parameters so that the desired transmission coefficients can be achieved over a wide bandwidth. When the quarter-wave metasurface is illuminated by an incident wave that is linearly polarized at 45° with respect to the major principal axis, the x - and y -polarizations are equally excited. Hence, we can choose a pattern for each metallic layer that exhibits distinctive equivalent parallel LC circuit behaviors along the x - and y -axes. It should be noted that here, the equivalent parallel LC circuit is chosen as an illustrative example, and the metallic pattern could also be in other forms including equivalent series LC circuit or purely inductive or capacitive circuits. For simplicity, it is assumed that all materials employed are lossless at this stage. Based on the assumptions above, the admittance tensor of the i th metallic layer can be written as

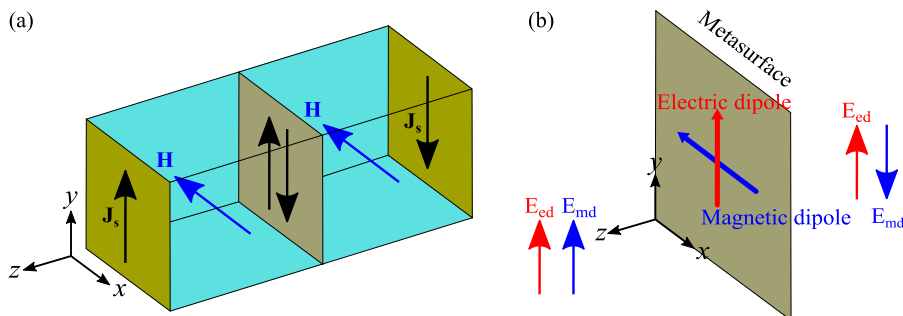


FIG. 1. Induced currents and electric field distributions of the metasurface. (a) Schematic diagram of the induced currents on the metasurface generated by a quasi-static magnetic field along the $-x$ -axis. The top and bottom layers are identical, and the dielectric spacers share the same thickness. (b) Sketch of the electric field distributions contributed from the electric and magnetic dipoles of equal strength.

$$\mathbf{Y}_{si} = \begin{bmatrix} \frac{1}{j\omega L_{xi}} + j\omega C_{xi} & 0 \\ 0 & \frac{1}{j\omega L_{yi}} + j\omega C_{yi} \end{bmatrix}, \quad (1)$$

where (L_{xi}, C_{xi}) and (L_{yi}, C_{yi}) are the pattern-equivalent inductance and capacitance along the x - and y -axes, respectively. The off-diagonal terms are equal to zero, indicating that there is no cross-coupling introduced by the pattern. Note that the analytical approach presented by Pfeiffer and Grbic solved for the optimal admittance at the design center frequency.^{27,36} However, the optimal admittance at the frequency of interest can be physically realized by a vast number of (L, C) combinations and hence diverse metallic patterns. Nevertheless, only very few metallic patterns are capable of providing a large bandwidth, enhanced efficiency, and high polarization purity performance. Hence, here, the frequency-dependent admittance is decomposed into the frequency-independent inductance and capacitance so as to numerically explore the metasurface dispersive performance within the frequency band of interest. The transfer matrix method is implemented to describe the scattering property of the anisotropic metasurface that comprises three metallic layers separated by two subwavelength dielectric spacers. These dielectric spacers can be modeled as transmission lines along the z -axis. Hence, the total 4×4 ABCD transfer matrix of the metasurface is given by³⁶

$$\begin{bmatrix} \mathbf{A} & \mathbf{B} \\ \mathbf{C} & \mathbf{D} \end{bmatrix} = \begin{bmatrix} \mathbf{I} & \mathbf{0} \\ \mathbf{nY}_{s1} & \mathbf{I} \end{bmatrix} \begin{bmatrix} \cos(kd)\mathbf{I} & -j\sin(kd)\eta_d\mathbf{n} \\ j\sin(kd)\eta_d^{-1}\mathbf{n} & \cos(kd)\mathbf{I} \end{bmatrix} \\ \times \begin{bmatrix} \mathbf{I} & \mathbf{0} \\ \mathbf{nY}_{s2} & \mathbf{I} \end{bmatrix} \begin{bmatrix} \cos(kd)\mathbf{I} & -j\sin(kd)\eta_d\mathbf{n} \\ j\sin(kd)\eta_d^{-1}\mathbf{n} & \cos(kd)\mathbf{I} \end{bmatrix} \\ \times \begin{bmatrix} \mathbf{I} & \mathbf{0} \\ \mathbf{nY}_{s1} & \mathbf{I} \end{bmatrix}, \quad (2)$$

where $\mathbf{I} = [1 \ 0; 0 \ 1]$ denotes the identity matrix and $\mathbf{n} = [0 \ -1; 1 \ 0]$ represents the 90° rotation matrix. The wavenumber and wave impedance of the dielectric spacer are denoted by k and η_d , respectively, while d is the dielectric spacer thickness. Each element in the final ABCD matrix is a 2×2 tensor corresponding to the x - and y -polarizations. It should be emphasized that here, only propagating modes are accounted. Evanescent modes resulting from the near-field coupling are assumed to be negligible, provided that electrically large spacings between the metallic layers are adopted. A small unit cell size together with a reasonably large layer spacing are beneficial to the accuracy of the analytical model.³⁶ Once the ABCD matrix is established, the S-parameters of the anisotropic metasurface under linearly polarized incident waves at normal incidence can be written as

$$\begin{bmatrix} \mathbf{S}_{11} & \mathbf{S}_{12} \\ \mathbf{S}_{21} & \mathbf{S}_{22} \end{bmatrix} = \begin{bmatrix} -\mathbf{I} & \frac{\mathbf{Bn}}{\eta_0} + \mathbf{A} \\ \frac{\mathbf{n}}{\eta_0} & \frac{\mathbf{Dn}}{\eta_0} + \mathbf{C} \end{bmatrix}^{-1} \begin{bmatrix} \mathbf{I} & \frac{\mathbf{Bn}}{\eta_0} - \mathbf{A} \\ \frac{\mathbf{n}}{\eta_0} & \frac{\mathbf{Dn}}{\eta_0} - \mathbf{C} \end{bmatrix}, \quad (3)$$

where \mathbf{S} is a 2×2 tensor for the x - and y -polarizations and η_0 is the free-space wave impedance. At this stage, the S-parameters of the anisotropic metasurface for two orthogonal linear polarizations can be readily calculated based on the equivalent inductances and capacitances of each metallic layer. Conversely, a stipulated S-parameter

specification can be obtained by implementing the genetic algorithm to determine the required circuit parameters.

To achieve circular polarization with high efficiency and high purity, the quarter-wave metasurface requires near-unity transmittances for the two orthogonal electric field components, i.e., $|S_{21}^{xx}|^2 = |S_{21}^{yy}|^2 = 1$, and a constant quadrature phase difference between them, i.e., $\angle S_{21}^{xx} - \angle S_{21}^{yy} = 90^\circ$. The possible range for the inductance and capacitance within a certain unit cell size is estimated based on the simulations of metallic patterns with equivalent parallel LC circuits along the x - and y -polarizations. Considering the feasibility for fabrication of a dielectric spacer and the assumption of negligible evanescent modes, a spacer thickness range from $100 \mu\text{m}$ to $200 \mu\text{m}$ is specified for the targeted frequency range between 220 GHz and 330 GHz. With the constraints identified, a cost function is assigned in the genetic algorithm to find the optimal $(L_{xi}, C_{xi}, L_{yi}, \text{ and } C_{yi})$ for the i th metallic layer and the desired thickness d for the dielectric spacers, with the aim of satisfying the objectives over a wide bandwidth. More specifically, the genetic algorithm starts from an initial group that consists of various individuals with genes formed by circuit parameters. Since the circuit parameters implemented here are frequency-independent, the scattering characteristics of the metasurface then can be numerically investigated over the frequency range of interest using Eqs. (1)–(3). Thus, the fitness of each parameter set is evaluated based on its scattering characteristics using the cost function. As such, the optimal circuit parameters are eventually selected to collectively achieve a transmission performance that closely approximates the objectives over the targeted frequency band.

III. RESULTS

Table I shows the calculated optimal inductances and capacitances for the quarter-wave metasurface provided by the outlined extended semi-analytical approach, while the thickness of each dielectric spacer is found to be $d = 195 \mu\text{m}$. Once the optimal set of $(L_{xi}, C_{xi}, L_{yi}, \text{ and } C_{yi})$ is determined for the i th metallic layer, a search for the corresponding physical structure is then conducted by designing a specific pattern to meet the optimal circuit parameters. Electromagnetic simulations are performed with the commercial software ANSYS HFSS. Figures 2(a) and 2(b) show the simulation settings to design each layer in the unit cell, where master-slave boundary conditions are employed in the transverse plane to imitate infinite periodicity. In order to avoid diffraction, a lattice constant of $540 \mu\text{m}$ is chosen, which corresponds to $0.5\lambda_0$ at the design center frequency of 275 GHz. Floquet ports are

TABLE I. Calculated optimal inductances and capacitances based on the extended semi-analytical approach. The units for inductances and capacitances are pH and fF, respectively.

| Top/bottom layer | | | | Middle layer | | | |
|------------------|----------|----------|----------|--------------|----------|----------|----------|
| x-axis | | y-axis | | x-axis | | y-axis | |
| L_{x1} | C_{x1} | L_{y1} | C_{y1} | L_{x2} | C_{x2} | L_{y2} | C_{y2} |
| 170.5 | 0.9 | 265.6 | 1.9 | 123.1 | 0.7 | 212.6 | 2.7 |

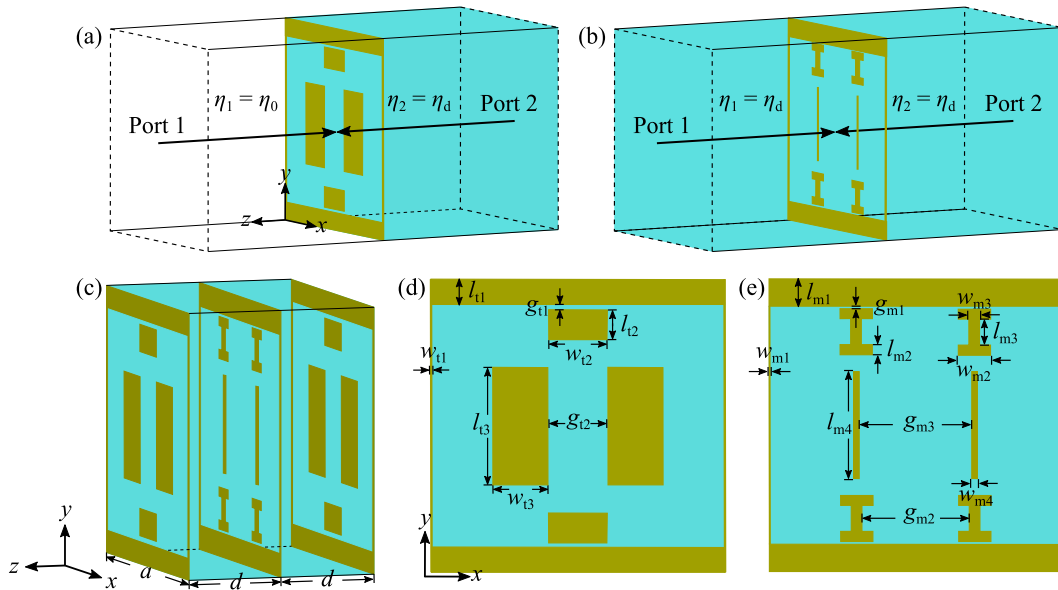


FIG. 2. Electromagnetic simulation settings for the physical realization of each metallic layer and geometry of the unit cell. (a) Top and bottom layer realizations and (b) middle layer realization. The top and bottom layers are at the interface between air and dielectric spacer, while the middle layer is hosted in between the dielectric spacers. The arrows indicate port de-embedding for phase compensation. (c) Unit cell 3D view, (d) top and bottom layers, and (e) middle layer. The top and bottom layers are identical to enhance the metasurface efficiency.

implemented to impose normally incident plane waves and also to collect the scattered waves. The Floquet ports are de-embedded to the metallic layer surface to acquire the intrinsic surface response independently from propagation effects in the media. In order to reduce the material losses, gold is utilized for the metallic layers and ultra-low loss cyclic olefin copolymer (COC) is applied for the dielectric spacers. The surface impedance of gold at terahertz frequencies is described by a Drude model,³⁷ while the COC dielectric spacer shows a relative permittivity of $\epsilon_r = 2.33$ and loss tangent of $\tan \delta = 0.0005$ from 220 GHz to 330 GHz.³⁸

To realize each metallic layer, the simulation starts from a pattern with arbitrary dimensions, but its equivalent circuits along the x - and y -axes are predominately parallel LC circuits. The pattern is then evolved to reproduce the optimal circuit parameters provided by the extended semi-analytical approach. The metallic pattern equivalent inductance and capacitance along the x - or y -polarization can be calculated based on the simulated admittances. For each metallic layer, the corresponding admittance tensor can be extracted from the simulated reflection coefficients by³⁶

$$Y_s = \left[\frac{I - S_{11}}{\eta_1} - \frac{I + S_{11}}{\eta_2} \right] [I + S_{11}]^{-1}, \quad (4)$$

where η_1 and η_2 are the wave impedances of the adjoining media. Hence, for each metallic layer and each polarization, the two unknowns of (L , C) can be analytically solved by retrieving the Y -parameters at two different frequencies. The equivalent inductance and capacitance are then compared with the optimal values from the semi-analytical approach, and the metallic pattern is altered

accordingly until the obtained simulated values match the optimal ones. Note that the physical realizations of the top and middle layers are carried out separately.

Figures 2(c), 2(d), and 2(e) plot the 3D structure of a quarter-wave metasurface unit cell. As mentioned, the top and bottom metallic layers are identical to enhance the efficiency, while the equivalent circuit of each metallic layer under the x - or y -polarization is basically a parallel LC circuit as implemented in the extended semi-analytical approach. Detailed dimensions of the structure are illustrated in Table II. Notably, a strip width of $4 \mu\text{m}$ ($w_{t1} = w_{m1} = 2 \mu\text{m}$) is desired at the unit cell borders to provide the optimal equivalent inductance under the y -polarization. Simulations suggest that the metasurface exhibits a large tolerance to the strip width variation

TABLE II. Detailed dimensions of the quarter-wave metasurface unit cell. The units are in μm .

| Parameter | Value | Parameter | Value | Parameter | Value |
|-----------|-------|-----------|-------|-----------|-------|
| a | 540 | w_{t3} | 101 | l_{m3} | 49 |
| d | 195 | g_{t1} | 10 | w_{m3} | 20 |
| l_{t1} | 47 | g_{t2} | 111 | l_{m4} | 198 |
| w_{t1} | 2 | l_{m1} | 50 | w_{m4} | 10 |
| l_{t2} | 54 | w_{m1} | 2 | g_{m1} | 5 |
| w_{t2} | 108 | l_{m2} | 18 | g_{m2} | 199 |
| l_{t3} | 216 | w_{m2} | 60 | g_{m3} | 209 |

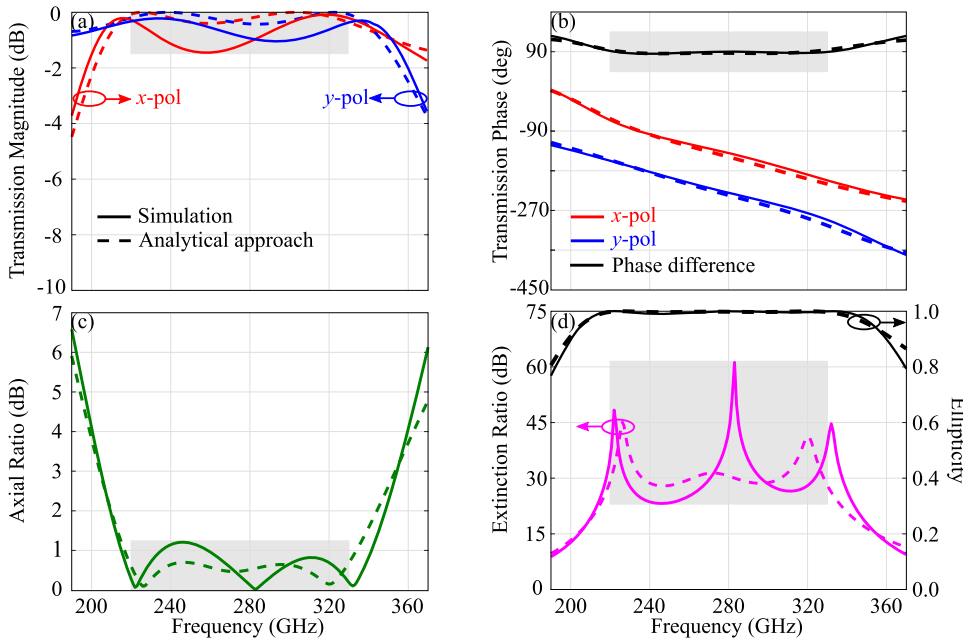


FIG. 3. Transmission coefficients and transmitted wave circular polarization purity of the quarter-wave metasurface provided by the semi-analytical approach and the 3D full-wave simulation. (a) Transmission magnitude, (b) transmission phase, (c) axial ratio, and (d) extinction ratio and ellipticity. The shaded area marks the frequency range of interest from 220 GHz to 330 GHz.

up to $w_{t1} = w_{m1} = 10 \mu\text{m}$. Figures 3(a) and 3(b) show the transmission coefficients of the quarter-wave metasurface as calculated using the extended semi-analytical approach and the 3D full-wave simulation. Since the calculation does not account for near-field coupling, the close agreement between the simulation and calculation results implies negligible coupling effects. Within the frequency range of interest from 220 GHz to 330 GHz, the maximum simulated insertion losses for the x - and y -polarizations are 1.45 dB and 1.04 dB, respectively, while the phase difference between the two components remains close to 90° . Moreover, simulations reveal that the reflection magnitudes for the x - and y -polarizations from 220 GHz to 330 GHz are less than -5.75 dB and -7.41 dB, respectively. Thus, the metasurface power loss is mainly contributed from reflections instead of material losses. However, the material losses considered in the simulation together with the deviation between the optimal and obtained equivalent inductances and capacitances collectively contribute to the discrepancy between the calculated and simulated results. Further simulations shown in supplementary A (supplementary material) suggest that the proposed design is relatively insensitive to tolerances in spacer thickness, as the relatively large electrical spacing between the metallic layers leads to a negligible near-field coupling. It is found that an axial ratio below 1.7 dB and a total efficiency above 64.6% can be maintained over the desired frequency band from 220 GHz to 330 GHz when the spacer thickness deviates by $\pm 20.5\%$.

The complex transmission coefficients presented by the semi-analytical approach and the 3D full-wave simulation suggest that the quarter-wave metasurface realizes linear-to-circular polarization conversion upon transmission. In order to rigorously quantify the performance of the quarter-wave metasurface, the axial ratio of the transmitted wave is evaluated. The axial ratio refers to the ratio of the major axis to the minor axis of the transmitted wave polarization ellipse, which can be written as³⁹

$$AR = \sqrt{\frac{E_{x0}^2 + E_{y0}^2 + [E_{x0}^4 + E_{y0}^4 + 2E_{x0}^2 E_{y0}^2 \cos(2\Delta\phi)]^{1/2}}{E_{x0}^2 + E_{y0}^2 - [E_{x0}^4 + E_{y0}^4 + 2E_{x0}^2 E_{y0}^2 \cos(2\Delta\phi)]^{1/2}}}, \quad (5)$$

where $E_{x0} = |S_{21}^{xx}|$ and $E_{y0} = |S_{21}^{yy}|$ are the transmission amplitudes of the x - and y -polarizations, respectively, and $\Delta\phi = \angle S_{21}^{xx} - \angle S_{21}^{yy}$ is the phase difference between them. It is possible to relate the axial ratio to the extinction ratio and the detailed derivation is shown in supplementary B (supplementary material). It is noted that the commonly used 3-dB axial ratio criterion corresponds to an extinction ratio of ~ 15 dB. To further evaluate the metasurface polarization conversion performance, the Stokes parameters of the transmitted wave is calculated using⁴⁰

$$\begin{aligned} S_0 &= |E_{x0}|^2 + |E_{y0}|^2, \\ S_1 &= |E_{x0}|^2 - |E_{y0}|^2, \\ S_2 &= 2|E_{x0}||E_{y0}|\cos(\Delta\phi), \\ S_3 &= 2|E_{x0}||E_{y0}|\sin(\Delta\phi). \end{aligned} \quad (6)$$

The output wave ellipticity is defined as $\chi = S_3/S_0$, where $\chi = 1$ indicates an ideal left-handed circularly polarized (LHCP) output wave, while $\chi = -1$ denotes a perfect right-handed circularly polarized (RHCP) output wave. Figures 3(c) and 3(d) depict the axial ratio, extinction ratio, and ellipticity of the transmitted wave obtained from the semi-analytical approach and simulation, revealing that a simulated 3-dB axial ratio fractional bandwidth of 53.3% can be sustained over a frequency range extending from 205 GHz to 354 GHz. Additionally, the simulated ellipticity from 220 GHz to 330 GHz is beyond 0.99, while the axial ratio remains lower than 1.21 dB that corresponds to an extinction ratio above 23.16 dB.

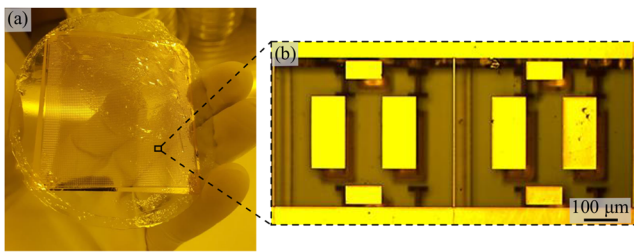


FIG. 4. Fabricated quarter-wave metasurface prototype. (a) Photograph of the fabricated sample and (b) magnified view containing two unit cells. The wrinkle part shown in (a) contains air bubbles introduced during the fabrication. The top layer is shifted $-24\ \mu\text{m}$ (4% of the unit cell size) along the x -axis and $48\ \mu\text{m}$ along the y -axis relative to the middle and bottom layers.

Images of the fabricated free-standing prototype are given in Fig. 4 and a slight top layer misalignment can be seen from Fig. 4(b), where the top layer is shifted $-24\ \mu\text{m}$ (4% of the unit cell size) along the x -axis and $48\ \mu\text{m}$ along the y -axis relative to the middle and bottom layers. Simulation results suggest that the quarter-wave

metasurface is robust to the slight top layer shift (see supplementary C of the [supplementary material](#)). The fabrication process is detailed in supplementary D ([supplementary material](#)), and it is also available in our previously reported linear polarization rotator design, which converts the linearly polarized incident waves to its orthogonal counterpart.⁴¹ To validate its performance, the manufactured quarter-wave metasurface is characterized using a Keysight Precision Network Analyzer (PNA) together with VDI WR-3.4 Extension Modules. We configure the extension modules so that they operate from 205 GHz to 340 GHz, which is beyond their typical frequency coverage of 220 GHz–330 GHz.⁴² As illustrated in Fig. 5(a), a vertically polarized incident wave is collimated by Lens 1 and then focused onto the sample after propagating through Lens 2. Lens 3 collimates the transmitted wave, while Lens 4 focuses the collimated wave onto the receiver. As a result, the fabricated sample with a size of $50 \times 50\ \text{mm}^2$ is illuminated by the incident beam with a focal spot of $\sim 1\ \text{mm}$ in diameter. In addition, the Rayleigh range of the incident beam equals 0.72 mm at the design center frequency of 275 GHz, and the three metallic layers are therefore included inside of the Rayleigh range of the focused beam. Thus, a normally incident plane wave illumination is assumed over the entire measurement

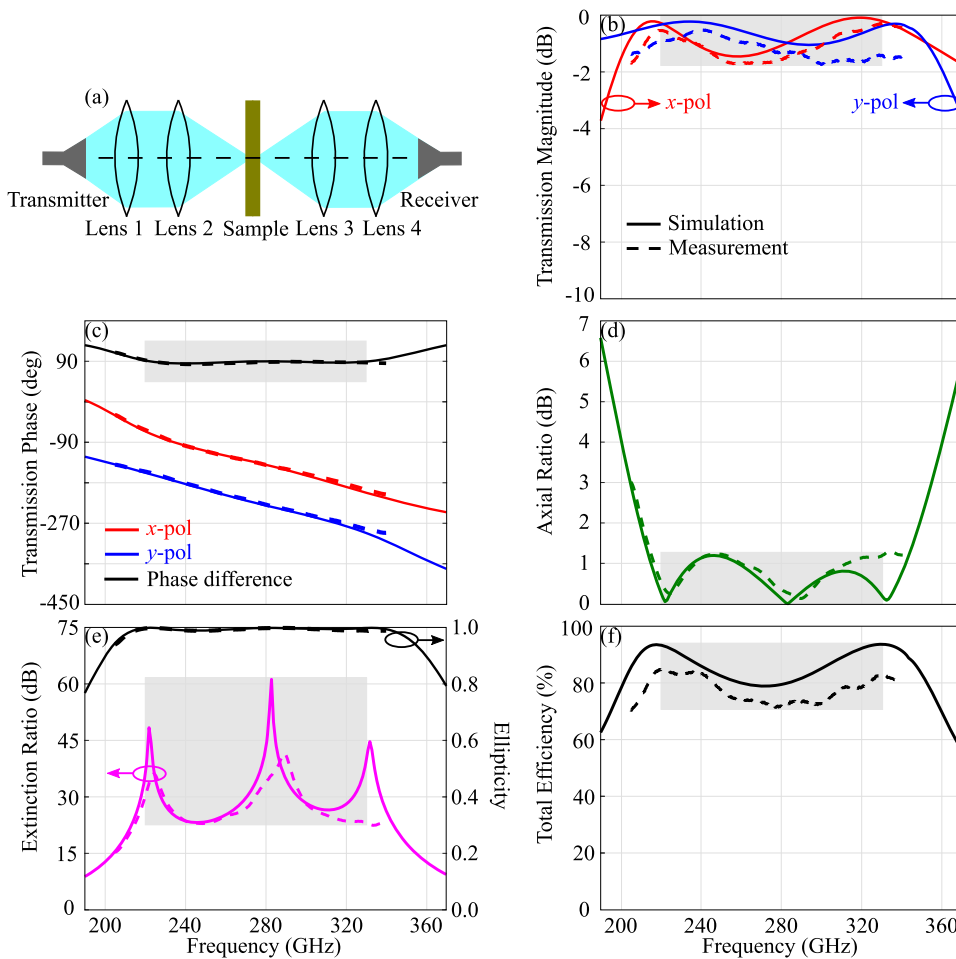


FIG. 5. Experimental setup and comparison between the simulated and measured results. (a) Schematic of the experimental setup using Keysight PNA and VDI WR-3.4 Extension Modules. Four lenses are used for collimating and focusing the beam. The measurement frequency band ranges from 205 GHz to 340 GHz. (b) Transmission magnitude, (c) transmission phase, (d) axial ratio, (e) extinction ratio and ellipticity, and (f) total efficiency. All transmission measurements are normalized against the reference measurement taken without the sample. The measured phase profiles for the x - and y -polarizations are offset by the constant value to coincide with simulations. The shaded area marks the frequency range of interest from 220 GHz to 330 GHz.

frequency range. The employed WR-3.4 metallic waveguides have a length of 25.4 mm, and in this waveguide, the cross-polarized wave manifested as the TE₀₁ mode is below its cutoff frequency. As a consequence, no polarizers are required to screen the cross-polarization component that experiences an attenuation of 31 dB/mm at 300 GHz in this waveguide. The transmission coefficients of the quarter-wave metasurface under the *x*- and *y*-polarizations are measured separately by rotating the sample. As a reference, a measurement is taken without the presence of sample.

Figures 5(b) and 5(c) depict the simulated and measured transmission coefficients of the quarter-wave metasurface, where a good agreement is confirmed. The measured results reveal that the maximum transmission loss is limited to 1.75 dB, and the phase difference between the *x*- and *y*-polarizations remains very close to 90°, leading to an axial ratio below 3 dB, an extinction ratio beyond 15 dB, and an ellipticity above 0.94 from 205 GHz to 340 GHz, as shown in Figs. 5(d) and 5(e), respectively. More specifically, the measured axial ratio from 220 GHz to 330 GHz is lower than 1.25 dB that corresponds to a measured extinction ratio beyond 22.88 dB, while the measured ellipticity is above 0.99. The maximum frequency in the measurements is constrained by the available characterization facility, but a general agreement with the simulation results is expected. The slight deviations between the measured and simulated results can be attributed to the unavoidable fabrication and experiment tolerances, the former of which could be dominant as suggested by further simulations. Moreover, Fig. 5(f) illustrates the total efficiency of the proposed design, accounting for the total transmittance of the *x*- and *y*-polarizations, i.e., $(|S_{21}^{xx}|^2 + |S_{21}^{yy}|^2)/2$. The simulated total efficiency from 205 GHz to 354 GHz is beyond 77.4%, while the measured total efficiency from 205 GHz to 340 GHz is above 70.2%, corresponding to a measured insertion loss below 1.54 dB. Additional simulations shown in supplementary E (supplementary material) reveal that an axial ratio below 2.2 dB from 220 GHz to 330 GHz can be effectively maintained up to an incidence angle of 10° in the *xoz* and *yo**z* incident

planes, but the corresponding simulated total efficiencies decrease to 72.7% and 62.6%, respectively. It is noted that the 45° polarized incident wave with respect to the *x*-axis gives LHCP output waves. RHCP waves can be obtained by rotating this structure by 90° around the *z*-axis. Importantly, the measured results further confirm that the proposed design is robust to the metallic layer shift, which is not uncommon in microfabrication of multilayer structures.

A performance comparison of the proposed work with notable existing designs from the literature is given in Table III. To simplify the comparison, a figure of merit is included to quantify the bandwidth and total efficiency collectively. It can be seen that the existing designs exhibit a modest figure of merit. In general, microwave-based quarter-wave plates basically show a higher figure of merit than those at terahertz frequencies as a result of a relatively low material loss and ease of fabrication at microwave frequencies. In the terahertz domain, most reported waveplates have limited bandwidth or efficiency, resulting in a remarkably low figure of merit. Comparing with the existing quarter-wave plates, our proposed design involves a systematic optimization methodology and provides an advantageous bandwidth, efficiency, and figure of merit. Importantly, the design can cover a full WR-3.4 waveguide frequency band from 220 GHz to 330 GHz,⁴² which is technologically significant and foreseen for terahertz point-to-point communications.³² Despite the restrictions in material and fabrication, the bandwidth and total efficiency of the metasurface are the highest among other broadband terahertz quarter-wave plates. In addition, a high output wave polarization purity with an axial ratio lower than 1.25 dB is achieved within the frequency band of interest. The metasurface bandwidth and efficiency enhancement can be attributed to the optimal frequency-independent circuit parameters provided by the extended semi-analytical approach, which can deliver a constant quadrature phase difference and high transmittances for the two orthogonal electric field components over a wide bandwidth. In addition, the tri-layer metasurface manipulates the electric and

TABLE III. Comparison between the proposed design and notable transmissive quarter-wave plates. FoM is the abbreviation of "Figure of Merit," representing the product of bandwidth and total efficiency. PEN indicates polyethylene naphthalate, while BCB denotes bisbenzocyclobutene.

| Structure | Metallic layers | Spacer material | Center frequency (GHz) | Bandwidth (AR < 3 dB) (%) | Minimum efficiency (%) | FoM (%) |
|-------------------------------------|-----------------|-----------------|------------------------|---------------------------|------------------------|---------|
| Microwave-based | | | | | | |
| Meander line and loop ⁴³ | 1 | Duroid 5880 | 24 | 47 | 50 | 24 |
| Cross strips ⁴⁴ | 2 | Taconic TLY-5 | 24 | 74 | 47 | 35 |
| Strip gratings ³⁵ | 5 | Duroid 5880 | 27 | 20 | 93 | 19 |
| Reactive surfaces ²⁶ | 6 | Duroid 6010 | 10 | 40 | 74 | 30 |
| Terahertz-based | | | | | | |
| Split slot ring ⁴⁵ | 1 | Silicon | 325 | 12 | 45 | 5 |
| Metal slots ²⁹ | 1 | PEN | 870 | 5 | 30 | 2 |
| Metal gratings ⁴⁶ | 2 | Polyimide | 1180 | 44 | 42 | 19 |
| Split ring resonators ²⁸ | 2 | BCB | 980 | 12 | 62 | 7 |
| This work | 3 | COC | 280 | 53 | 70 | 37 |

magnetic dipoles separately, further contributing to the efficiency improvement that cannot be achieved by the single- and bi-layer designs, as presented in Table III.

IV. CONCLUSION

A broadband terahertz quarter-wave plate that allows linear-to-circular polarization conversion is constructed on the basis of metasurfaces. The device is developed and optimized using an extended semi-analytical approach that targets broadband and high-efficiency performance. A measured axial ratio of less than 3 dB can be sustained from 205 GHz to at least 340 GHz, where the highest frequency is limited by the measurement facility. In addition, the proposed design demonstrates its robustness to the metallic layer misalignments. A misaligned fabricated prototype with its top layer shifted -4% of the unit cell size along the x -axis and 8% of the unit cell size along the y -axis shows a close transmission performance with the aligned structure. As such, the proposed metasurface relaxes the fabrication requirements at terahertz frequencies. The extended semi-analytical approach can be readily implemented to design various bandwidth-enhanced transmissive metasurfaces for wavefront control and polarization manipulation.

SUPPLEMENTARY MATERIAL

See the [supplementary material](#) for further details.

AUTHORS' CONTRIBUTIONS

X.Y. and R.T.A. contributed equally to this work.

ACKNOWLEDGMENTS

This research was supported by Australian Research Council Discovery Projects (Grant Nos. ARC DP170101922 and DP180103561). X.Y. acknowledges the Ph.D. scholarship support from the China Scholarship Council (CSC) (Grant No. 201606270204). This work was performed, in part, at the Micro Nano Research Facility at RMIT University and the Melbourne Center for Nanofabrication (MCN) in the Victorian Node of the Australian National Fabrication Facility (ANFF).

DATA AVAILABILITY

The data that support the findings of this study are available from the corresponding author upon reasonable request.

REFERENCES

- P. H. Siegel, *IEEE Trans. Microwave Theory Tech.* **50**, 910–928 (2002).
- H.-J. Song and T. Nagatsuma, *IEEE Trans. Terahertz Sci. Technol.* **1**, 256–263 (2011).
- W. Withayachumnankul, R. Yamada, M. Fujita, and T. Nagatsuma, *APL Photonics* **3**, 051707 (2018).
- C. B. Reid, E. Pickwell-MacPherson, J. G. Laufer, A. P. Gibson, J. C. Hebden, and V. P. Wallace, *Phys. Med. Biol.* **55**, 4825–4838 (2010).
- T. C. Bowman, M. El-Shenawee, and L. K. Campbell, *IEEE Trans. Antennas Propag.* **63**, 2088–2097 (2015).
- K. Kawase, Y. Ogawa, Y. Watanabe, and H. Inoue, *Opt. Express* **11**, 2549–2554 (2003).
- M. Mittendorff, S. Li, and T. E. Murphy, *ACS Photonics* **4**, 316–321 (2017).
- J.-S. Li, Y. Li, and L. Zhang, *IEEE Photonics Technol. Lett.* **30**, 238–241 (2018).
- Y. S. Cao, L. J. Jiang, and A. E. Ruehli, *IEEE Trans. Antennas Propag.* **64**, 1385–1393 (2016).
- D. Grischkowsky, S. Keiding, M. van Exter, and C. Fattinger, *J. Opt. Soc. Am. B* **7**, 2006–2015 (1990).
- Z. Chen, Y. Gong, H. Dong, T. Notake, and H. Minamide, *Opt. Commun.* **311**, 1–5 (2013).
- M. Reid and R. Fedosejevs, *Appl. Opt.* **45**, 2766–2772 (2006).
- M. Nagai, N. Mukai, Y. Minowa, M. Ashida, J. Takayanagi, and H. Ohtake, *Opt. Lett.* **39**, 146–149 (2014).
- U. Levy and Y. Fainman, *J. Opt. Soc. Am. A* **21**, 881–889 (2004).
- A. Hu, F. Chu, C. Guo, G. Li, and J. Wu, *Optik* **163**, 120–125 (2018).
- H. Shi and Y. Hao, *Opt. Express* **26**, 20132–20144 (2018).
- D. Headland, E. Carrasco, S. Nirantar, W. Withayachumnankul, P. Gutruf, J. Schwarz, D. Abbott, M. Bhaskaran, S. Sriram, J. Perruisseau-Carrier, and C. Fumeaux, *ACS Photonics* **3**, 1019–1026 (2016).
- C.-C. Chang, D. Headland, D. Abbott, W. Withayachumnankul, and H.-T. Chen, *Opt. Lett.* **42**, 1867–1870 (2017).
- T. Niu, W. Withayachumnankul, B. S.-Y. Ung, H. Menekse, M. Bhaskaran, S. Sriram, and C. Fumeaux, *Opt. Express* **21**, 2875–2889 (2013).
- Y. Monnai, D. Jahn, W. Withayachumnankul, M. Koch, and H. Shinoda, *Appl. Phys. Lett.* **106**, 021101 (2015).
- Y. Z. Cheng, W. Withayachumnankul, A. Upadhyay, D. Headland, Y. Nie, R. Z. Gong, M. Bhaskaran, S. Sriram, and D. Abbott, *Appl. Phys. Lett.* **105**, 181111 (2014).
- W. S. L. Lee, R. T. Ako, M. X. Low, M. Bhaskaran, S. Sriram, C. Fumeaux, and W. Withayachumnankul, *Opt. Express* **26**, 14392–14406 (2018).
- R. T. Ako, W. S. L. Lee, M. Bhaskaran, S. Sriram, and W. Withayachumnankul, *APL Photonics* **4**, 096104 (2019).
- R.-H. Fan, Y. Zhou, X.-P. Ren, R.-W. Peng, S.-C. Jiang, D.-H. Xu, X. Xiong, X.-R. Huang, and M. Wang, *Adv. Mater.* **27**, 1201–1206 (2015).
- D. Blanco and R. Sauleau, *IEEE Trans. Antennas Propag.* **66**, 1874–1881 (2018).
- S. M. A. Momeni Hasan Abadi and N. Behdad, *IEEE Trans. Antennas Propag.* **64**, 525–534 (2016).
- C. Pfeiffer and A. Grbic, *IEEE Trans. Microwave Theory Tech.* **61**, 4407–4417 (2013).
- Z. Han, S. Ohno, Y. Tokizane, K. Nawata, T. Notake, Y. Takida, and H. Minamide, *Opt. Lett.* **43**, 2977–2980 (2018).
- D. Wang, Y. Gu, Y. Gong, C.-W. Qiu, and M. Hong, *Opt. Express* **23**, 11114–11122 (2015).
- N. Yu, F. Aieta, P. Genevet, M. A. Kats, Z. Gaburro, and F. Capasso, *Nano Lett.* **12**, 6328–6333 (2012).
- B. Yang, W.-M. Ye, X.-D. Yuan, Z.-H. Zhu, and C. Zeng, *Opt. Lett.* **38**, 679–681 (2013).
- IEEE standard for high data rate wireless multi-media networks—amendment 2: 100 Gb/s wireless switched point-to-point physical layer, IEEE Std 802.15.3d-2017 (Amendment to IEEE Std 802.15.3-2016 as amended by IEEE Std 802.15.3e-2017), 1–55, 2017.
- M. Decker, I. Staude, M. Falkner, J. Dominguez, D. N. Neshev, I. Brener, T. Pertsch, and Y. S. Kivshar, *Adv. Opt. Mater.* **3**, 813–820 (2015).
- S. L. Jia, X. Wan, D. Bao, Y. J. Zhao, and T. J. Cui, *Laser Photonics Rev.* **9**, 545–553 (2015).
- V. M. Shalaev, W. Cai, U. K. Chettiar, H.-K. Yuan, A. K. Sarychev, V. P. Drachev, and A. V. Kildishev, *Opt. Lett.* **30**, 3356–3358 (2005).
- C. Pfeiffer and A. Grbic, *Phys. Rev. Appl.* **2**, 044011 (2014).
- D. Hashimshony, I. Geltner, G. Cohen, Y. Avitzour, A. Zigler, and C. Smith, *J. Appl. Phys.* **90**, 5778–5781 (2001).
- K. Nielsen, H. K. Rasmussen, A. J. Adam, P. C. Planken, O. Bang, and P. U. Jepsen, *Opt. Express* **17**, 8592–8601 (2009).
- C. A. Balanis, *Antenna Theory: Analysis and Design* (John Wiley & Sons, 2016).
- W. H. McMaster, *Am. J. Phys.* **22**, 351–362 (1954).

⁴¹R. T. Ako, W. S. L. Lee, S. Atakaramians, M. Bhaskaran, S. Sriram, and W. Withayachumnankul, *APL Photonics* **5**, 046101 (2020).

⁴²J. Hesler, A. Kerr, W. Grammer, and E. Wollack, in Proceedings of the 18th International Symposium on Space Terahertz Technology, 2007.

⁴³P. Fei, Z. Shen, X. Wen, and F. Nian, *IEEE Trans. Antennas Propag.* **63**, 4609–4614 (2015).

⁴⁴H. B. Wang, Y. J. Cheng, and Z. N. Chen, *IEEE Trans. Antennas Propag.* **68**, 1186–1191 (2020).

⁴⁵M. Euler, V. Fusco, R. Cahill, and R. Dickie, *IEEE Trans. Antennas Propag.* **58**, 2457–2459 (2010).

⁴⁶L. Cong, N. Xu, J. Gu, R. Singh, J. Han, and W. Zhang, *Laser Photonics Rev.* **8**, 626–632 (2014).



Minerva Access is the Institutional Repository of The University of Melbourne

Author/s:

You, X; Ako, RT; Lee, WSL; Bhaskaran, M; Sriram, S; Fumeaux, C; Withayachumnankul, W

Title:

Broadband terahertz transmissive quarter-wave metasurface

Date:

2020-09-01

Citation:

You, X., Ako, R. T., Lee, W. S. L., Bhaskaran, M., Sriram, S., Fumeaux, C. & Withayachumnankul, W. (2020). Broadband terahertz transmissive quarter-wave metasurface. *APL PHOTONICS*, 5 (9), <https://doi.org/10.1063/5.0017830>.

Persistent Link:

<http://hdl.handle.net/11343/280482>

File Description:

Published version

License:

CC BY